JGR Space Physics

RESEARCH ARTICLE
10.1029/2019JA026792

Magnetosphere-Ionosphere-Thermosphere Coupling at Jupiter Using a Three-Dimensional Atmospheric General Circulation Model

J. N. Yates[1,2], L. C. Ray[3], N. Achilleos[4,5], O. Witasse[6], and N. Altobelli[1]

[1]ESAC, European Space Agency, Madrid, Spain, [2]Department of Physics, Imperial College London, London, UK, [3]Department of Physics, Lancaster University, Lancaster, UK, [4]Department of Physics and Astronomy, University College London, London, UK, [5]Centre for Planetary Science, UCL-Birkbeck, London, UK, [6]European Space Agency, ESTEC, Noordwijk, Netherlands

Key Points:
- A new model of Jupiter's magnetosphere-ionosphere-thermosphere coupling is presented
- This new 3-D model demonstrates the importance of including zonal terms in the momentum and energy equations
- The high-latitude temperatures are comparable to the lower range of observed temperatures

Correspondence to:
J. N. Yates,
japheth.yates@gmail.com

Citation:
Yates, J. N., Ray, L. C., Achilleos, N., Witasse, O. G., & Altobelli, N. (2020). Magnetosphere-ionosphere-thermosphere coupling at Jupiter using a three-dimensional atmospheric general circulation model. *Journal of Geophysical Research: Space Physics*, *125*, e2019JA026792. https://doi.org/10.1029/2019JA026792

Received 2 APR 2019
Accepted 8 SEP 2019
Accepted article online 14 OCT 2019

Abstract Jupiter's upper atmosphere is ~ 700 K hotter than predicted based on solar extreme ultraviolet heating alone. The reason for this still remains a mystery and is known as the "energy crisis." It is thought that the interaction between Jupiter and its dynamic magnetosphere plays a vital role in heating its atmosphere to the observed temperatures. Here, we present a new model of Jupiter's magnetosphere-ionosphere-thermosphere-coupled system where we couple a three-dimensional atmospheric general circulation model to an axisymmetric magnetosphere model. We find that the model temperatures are on average ~60 K, with a maximum of ~200 K, hotter than the model's two-dimensional predecessor making our high-latitude temperatures comparable to the lower limit of observations. Stronger meridional winds now transport more heat from the auroral region to the equator increasing the equatorial temperatures. However, despite this increase, the modeled equatorial temperatures are still hundreds of kelvins colder than observed. We use this model as an intermediate step toward a three-dimensional atmospheric model coupled to a realistic magnetosphere model with zonal and radial variation.

1. Introduction

The solar system's giant planets all have very hot upper atmospheres. Their atmospheres are much hotter than would be expected if they were heated primarily by solar extreme ultraviolet radiation (EUV) like the terrestrial upper atmosphere. Jupiter's thermosphere is ~ 700 K (~ 4.5 times) hotter than predicted (e.g., Seiff et al., 1998; Strobel & Smith, 1973; Yelle & Miller, 2004). The other giant planets Saturn, Uranus, and Neptune are respectively ~ 2.5, ~ 5.8, and ~ 4.5 times hotter than predicted. This is known as the giant planet energy crisis. To date, we still cannot explain the source of these high temperatures despite many attempts. The high thermospheric temperatures at Jupiter are thought to be caused by (i) the interaction between its upper atmosphere and magnetosphere via Joule heating (Millward et al., 2005; Smith et al., 2005; Waite et al., 1983), ion drag (Miller et al., 2000; Millward et al., 2005; Smith et al., 2005) and particle precipitation—be it auroral (Grodent et al., 2001; Waite et al., 1983) or middle and low latitude (Yelle & Miller, 2004); (ii) the breaking of acoustic and/or gravity waves in the upper atmosphere (Young et al., 1997; Matcheva & Strobel, 1999; Hickey et al., 2000; Schubert et al., 2003); or (iii) by some combination of both. The Galileo probe's descent into Jupiter's atmosphere remains the only potential in situ evidence of Jovian atmospheric waves (Young et al., 1997). Combined with the fact that such waves are difficult to detect remotely it is complicated to quantify and confirm the plethora of waves and wave modes that can be sustained within Jupiter's atmosphere. Recently, Müller-Wodarg et al. (2019) discovered atmospheric waves present in Saturn's thermosphere. The authors found that these waves may be damped and as such could enhance the eddy friction resulting in an increase in atmospheric temperature. Due to the similarity between Jupiter and Saturn such damped waves could also be present in the Jovian system and should be considered in future studies. In this study, we therefore focus solely on the magnetospheric interaction.

The interaction between a planet's upper atmosphere, consisting of an ionosphere embedded in a neutral thermosphere, and magnetosphere is known as magnetosphere-ionosphere-thermosphere (MIT) coupling. This coupled system is investigated using numerical models, where the neutral atmosphere is represented by a general circulation model (GCM), which is coupled to either a simplified model representing the currents

in the magnetosphere-ionosphere (MI) system (Ray et al., 2015; Smith & Aylward, 2009; Tao et al., 2009, 2010, 2014; Yates et al., 2012, 2014, 2018) or by imposing electric fields directly into the thermospheric GCM (Achilleos et al., 1998, 2001; Bougher et al., 2005; Majeed et al., 2005, 2009, 2016; Millward et al., 2002, 2005). The Jovian Ionosphere Model (JIM; Achilleos and Millward) and the Jupiter Thermospheric GCM (JTGCM; Bougher and Majeed) are models that investigated the 3-D dynamics and chemistry of Jupiter's upper atmosphere and its MIT coupling. The JIM model was the first Jovian 3-D MIT coupling model employing an offset tilted dipole magnetic field model and an Earth-like parameterization of Jupiter's ionospheric electric field. JIM investigated the creation of Jupiter's ionosphere within the auroral region and how ionospheric ion motion influenced the thermospheric neutrals. JTGCM simulates MIT coupling by using terrestrial parameterizations of ion drag and Joule heating and ion drifts generated using a convection electric field model based on Voyager measurements. Joule heating is then scaled down until the model reproduces the observed temperatures. Both JIM and JTGCM model how the neutral winds are modified by their coupling with Jupiter's ionospheric ions and the resulting redistribution of heat from the auroral regions to lower latitudes. The resulting neutral flows amount to a subcorotational (westward) zonal jet at high latitudes, equatorward high-altitude flows, and poleward flows in the high-latitude and low-altitude thermosphere. JTGCM's flows are, however, very asymmetric in coverage and speeds due to their use of the VIP4 (Connerney et al., 1998) magnetic field model instead of a simple tilted-dipole field, and some may argue that this is more realistic.

The 3-D models presented above impose magnetospheric forcing in the polar regions but do not self-consistently couple the magnetosphere to the upper atmosphere. Self-consistently coupling the magnetosphere and ionosphere-thermosphere allows the field-aligned currents (FACs) to affect the magnetospheric convection electric field and magnetospheric plasma. A series of models were subsequently developed to self-consistently include such coupling. Due to the complexity of such coupling the models were designed to initially be axisymmetric. The Smith and Aylward (2009), Tao et al. (2009), Ray et al. (2015), and Yates et al. (2014) models all consist of a one-dimensional (1-D) magnetosphere model self-consistently coupled to a two-dimensional (2-D) atmospheric GCM. Of all the 2-D coupled MIT models, only the Tao et al. models could reproduce atmospheric temperatures comparable to those observed at all latitudes by including heating terms due to acoustic waves as parameterized by Schubert et al. (2003). The other 2-D models did not include heating due to acoustic wave breaking for reasons given above. This means that their temperatures, particularly, at equatorial latitudes, were modeled to be much lower ($\sim$ 300 K) than observed ($\sim$ 900 K). It is worth noting that the Smith et al. model can reproduce the observed temperatures if the authors include an extra, low-latitude, Joule heating term due to fluctuating electric fields. Regarding neutral dynamics, the suite of 2-D models found similar flow cells to those found using the 3-D models albeit with generally lower meridional velocities. Most MIT coupling studies assume that the system is in quasi-equilibrium (or steady state). The works of Yates et al. (2014), Tao et al. (2014), and Yates et al. (2018) were the first to include time dependence outside of the thermospheric GCM by either having a time-dependent magnetospheric size (Yates et al., 2014, 2018) or solar EUV flux (Tao et al., 2014). Including variable solar EUV fluxes (factors of 1 to 3) results in moderate thermospheric temperature ($\sim$ 10 K) and neutral velocity ($\sim$20%) increases while large changes in magnetospheric size ($\sim$ 40 R_J; Jovian radii with 1 R_J = 71,492 km) lead to temperature variations of a few tens of Kelvin. Moreover, varying the size of the magnetosphere leads to an increase in equatorward transport of heat, which is typically prohibited in the steady-state simulations pertaining to Jupiter and Saturn (e.g., Smith & Aylward, 2008, 2009). If we exclude the effect of wave heating, the time-dependent additions discussed above have been unable to reproduce the observed temperatures despite adding considerable complexity to the MIT coupling models.

This study presents results from a newly developed Jovian 3-D thermospheric GCM self-consistently coupled to a 1-D magnetosphere model. We describe our coupled model including its limitations in section 2 and present our simulation results while comparing them to its 2-D progenitor model (Yates et al., 2014) in section 3. In section 4 we discuss how the new model compares to available observations and previous Jovian 3-D models. We summarize and conclude in section 5.

2. Model Description

The coupled MIT steady-state model presented here is largely based on that presented in numerous studies (e.g., Ray et al., 2015; Smith & Aylward, 2009; Yates et al., 2014) and as such we will briefly summarize the model below and introduce the new components that have been added for this study.

2.1. Thermosphere Model

The thermosphere model here is a GCM solving the full time-dependent nonlinear three-dimensional (3-D) Navier-Stokes equations of energy, momentum, and continuity, using explicit time integration (Müller-Wodarg et al., 2006) with a time step of 3 s. The model has been developed from the 2.5-D (2.5-D because zonal gradients in the Navier-Stokes equations are not included) azimuthally symmetric GCM of Smith and Aylward (2009) to fully include the third dimension. Our new model solves the Navier-Stokes equations in a spherical-pressure coordinate system, providing time-dependent distributions of thermospheric wind, temperature, and energy. The horizontal (zonal and meridional) momentum, energy, and continuity equations, which we solve can be found in Achilleos et al. (1998) or Müller-Wodarg et al. (2006). We assume hydrostatic equilibrium in our model so the full vertical momentum equation is not solved. Our model is resolved on a 0.2° latitude, 10° longitude, and 0.4 pressure scale height grid, with a lower boundary at 2μbar (300 km above the 1 bar [B] level) and an upper boundary at 0.02 nbar.

2.2. Ionosphere Model

The ionosphere model we employ is the same as that described in Yates et al. (2014) and Yates et al. (2018). The model is separated into two parts: (i) a vertical part describing the relative change of conductivity with altitude (Grodent et al., 2001); and (ii) a horizontal part, which scales the vertical conductivity profiles such that the height-integrated Pedersen conductance Σ_P is equal to the fixed values that we prescribe. The only difference between this ionospheric model and that in Yates et al. (2018) is that here we have day-night variation in Σ_P. In this 3-D model we have four fixed conductance regions:

1. polar regions ($|\theta| > 74°$) with $\Sigma_P = 0.2$ mho (Isbell et al., 1984);
2. auroral region ($|\theta| = 60–74°$) with $\Sigma_P = 0.5$ mho (Nichols, 2011; Yates et al., 2014);
3. dayside low-latitude region ($-60° \leq \theta \leq 60°$) with $\Sigma_P = 0.0275$ mho (Hill, 1980);
4. nightside low-latitude region ($-60° \leq \theta \leq 60°$) with $\Sigma_P = 0.0$ mho.

The conductance in the nightside low-latitude (Region 4 above) region is set to 0. The conductivity model employed in this study basically consists of conductances due to solar EUV radiation (Region 3) and enhancements due to particle precipitation in the high-latitude regions (Regions 1 and 2). Solar EUV does not reach the nightside ionosphere, and so the conductance at low latitudes depends on the lifetime of the ionospheric species and whether low-latitude particle precipitation is present. For simplicity, we assume that there is no low-latitude particle precipitation and that the lifetime of ionospheric species is small enough so that there is zero conductance on the nightside. This assumption does not influence the atmosphere as such as is investigated in this study. A future study will incorporate a more realistic nightside ionospheric conductance.

2.3. Magnetosphere Model

We use the same magnetosphere model described in Smith and Aylward (2009) and Yates et al. (2012, 2014, 2018), which is based on the works of Nichols and Cowley (2004), Cowley et al. (2005), and Cowley et al. (2007). The model is axisymmetric, aligned with Jupiter's rotation axis, and solves for the magnetospheric plasma angular velocity. Additionally, it allows for the magnetic mapping between the magnetosphere and ionosphere. This mapping is achieved by assuming that surfaces of constant flux function form shells of magnetic field lines with common magnetospheric equatorial radial distances ρ_e and ionospheric colatitude θ_i. As such, one can equate the ionospheric flux function $F_i(\theta_i)$ with its magnetospheric equivalent $F_e(\rho_e)$ (magnetic flux integrated between a given ρ_e and infinity) giving

$$F_i(\theta_i) = B_J R_i^2 sin^2\theta_i = F_e(\rho_e). \quad (1)$$

where $B_J = 426\,400$ nT (Connerney et al., 1998) and is the equatorial magnetic field strength at the planet's surface. R_i is the ionospheric radius, which for this study we set to R_J. $F_e(\rho_e)$ (and the corresponding equatorial magnetic field) are taken from Nichols and Cowley (2004).

2.4. Coupled MIT Model

Our three model components are coupled as shown in Figure 1a. The atmospheric module solves the time-dependent Navier-Stokes equations before passing an "effective" thermospheric angular velocity Ω_T to the magnetosphere module. Ω_T is the weighted average of all the horizontal winds and is the thermospheric neutral velocity that the magnetosphere sees (see Smith & Aylward, 2008, 2009, for details on how this is calculated). The magnetosphere module solves for the steady-state magnetospheric plasma angular velocity Ω_M using the Hill-Pontius equation (Hill, 1979; Pontius, 1997; Pontius & Hill, 1982), which balances the

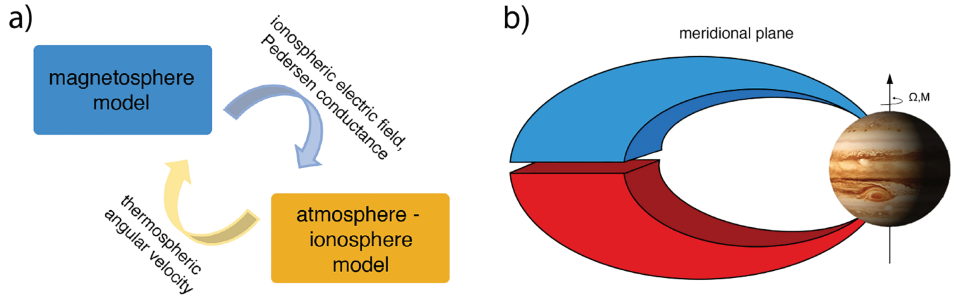

Figure 1. (a) Diagram representing our coupled magnetosphere-ionosphere-thermosphere model. (b) Schematic showing the separate magnetosphere models for each magnetic hemisphere which couple to the thermosphere model.

torque between the outward diffusion of iogenic plasma in the magnetosphere and the $\mathbf{J} \times \mathbf{B}$ force associated with magnetosphere-ionosphere currents (Yates et al., 2012). These two angular velocities combined with the height-integrated Pedersen conductance from the ionosphere module enable us to self-consistently determine the MI coupling currents and the resultant heating of the atmosphere due to the magnetospheric interaction. The full details on how these modules are coupled together can be found in Smith and Aylward (2009), Yates et al. (2012, 2014), and Ray et al. (2015). In this new 3-D model the northern and southern magnetospheric hemispheres are solved separately and then combined in the thermosphere module. We also only couple the noon local time (LT)/longitude grid points of the thermosphere to our magnetosphere model and then impose the resulting magnetospheric currents to the other longitudes of the thermosphere. The noon LT coupling is schematically shown in Figure 1b. The limitations of our current approach are discussed below.

2.5. Limitations of the Current Model

Given that this model is built on the previous models of Smith and Aylward (e.g., 2009) and Yates et al. (e.g., 2014), it also shares some of their limitations. We begin by briefly describing some of the common limitations before discussing limitations, which are particular to the current model.

1. Using fixed Pedersen conductances in the auroral region (±60–74° latitude). Works by Yates et al. (2012, 2014) have shown that using a fixed Pedersen conductance, instead of a variable one, in this region does not significantly alter the local thermospheric dynamics and heating if we consider perfect coupling between the ionosphere and magnetosphere, that is, there are no field-aligned potential (FAP) drops. We also employ a fixed, albeit smaller, Pedersen conductance poleward of the auroral region. The ionosphere and precipitating particles in this region are only recently being investigated by Jupiter's polar orbiting Juno spacecraft which will undoubtedly shed light on the conditions in this relatively unexplored region of Jupiter's upper atmosphere and high-latitude magnetosphere. The dayside and nightside equatorial regions have little, if any, MI coupling there so having a fixed conductivity in these regions will not influence the coupled model.
2. Using a fixed magnetospheric plasma angular velocity profile mapping to Jupiter's outer magnetosphere (±74–80° latitude) and polar cap (> ±80° latitude). We employ fixed estimates of Jupiter's magnetospheric plasma flow (based on works by Isbell et al., 1984; Cowley et al., 2005) in these regions due to the limited amount of measurements taken in Jupiter's distant magnetosphere. Recent work by Johnson et al. (2017) has shown that there is a strongly subcorotating (~<20%) ion flow region possibly mapping to the distant magnetosphere. Therefore, we continue to use these fixed flow assumptions to allow comparison with older models and until further observations are available.
3. No FAP development. In this work we do not allow for the development of FAP drops resulting in the decoupling between the ionospheric and magnetospheric flows—we assume perfect MI coupling. Work by Ray et al. (2015) was the first to include FAPs in a MIT coupling model and found that neutral temperatures and flows were changed by a few percent when compared to the same MIT model without FAPs. The variation in the Pedersen conductance due to its self-consistent formulation was found to have a greater influence on the thermosphere.

Our model uses a full 3-D thermospheric GCM and ideally this would be coupled to a full 3-D magneto-hydrodynamic magnetosphere model, but this is currently too computationally expensive to carry out any

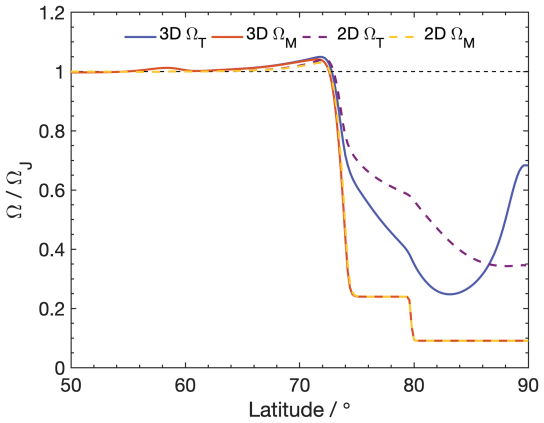

Figure 2. Three-dimensional (solid lines) and 2-D (dashed lines) thermospheric (blue and purple lines) and magnetospheric (red and yellow lines) angular velocity profiles as a function of latitude.

feasible studies. Simplifications of the MIT system therefore need to be made to allow for reasonable computation times. As discussed in section 2.4, our approach is to couple our axisymmetric magnetosphere model (based on Yates et al., 2014) to the noon LT slice of the thermosphere assuming that the magnetosphere is aligned with Jupiter's rotation axis. We solve for the northern and southern magnetosphere separately before combining the results in the thermosphere. We then project and impose the magnetospheric output at all other LT/longitudes. The result is a 3-D GCM coupled to a magnetosphere with no zonal variation. This is not physically realistic as Jupiter's magnetosphere shows much LT variation (e.g., Connerney et al., 2018; Khurana, 2001; Ray et al., 2014). However, we do believe this model to be a suitable intermediate step toward a more comprehensive and self-consistent 3-D MIT coupled model. It allows us to investigate the influence of gradually increasing the complexity of the coupled system.

2.6. Angular Velocity Profiles

In this study we present two simulations, one using a two-dimensional atmosphere model (Yates et al., 2014) and the other using the new three-dimensional atmospheric GCM described above. Both simulations employ a magnetodisc size of 65 R_J with all parameters kept equal. The simulations have been run for 500 rotations and have achieved steady state.

The normalized thermospheric and magnetospheric angular velocities discussed above are plotted as a function of atmospheric latitude in Figure 2. Solid lines show the new 3-D output and dashed lines show 2-D output from Yates et al. (2014) for comparison. Thermospheric angular velocities are shown in blue and purple lines while magnetospheric angular velocities are shown in red and yellow lines. Magnetospheric angular velocities essentially remain unchanged between the 2-D and 3-D models due to the similarities in the magnetosphere model. The thermospheric angular velocities, however, differ, particularly for latitudes poleward of 75°. These polar regions subcorotate to a larger degree in the 3-D simulation compared to the 2-D one until ~ 86° where 3-D velocities increase to ~70% of corotation. This highlights the difference between using an axisymmetric atmospheric GCM and a full 3-D one, which will be discussed in more detail below.

3. Simulation Results: 3-D and 2-D Comparison

3.1. Atmospheric Dynamics

Figure 3 compares neutral wind velocities between our new 3-D (Figures 3d–3f) simulation and an equivalent 2-D northern hemisphere (Figures 3a–3c) steady-state simulation (Yates et al., 2014). Figures 3a and 3d show the zonal (east-west) winds in the corotation frame as a function of pressure and latitude. Figures 3b and 3e show meridional (north-south) winds and Figures 3c and 3f show vertical (up-down) winds respectively as a function of pressure and latitude. The structure of the neutral winds remains almost unchanged between our 2-D and 3-D simulations. The 3-D zonal winds show strong subcorotating (blue colors) jets in the polar regions (latitudes >75°) and also weaker subcorotating jets at midlatitudes. Supercorotating (black contour) jets are also seen at low altitudes in each simulation. In our 2-D simulation the winds are more corotational (subcorotating and supercorotating to a lesser degree). The meridional winds consist of strong poleward flows (blue) at high latitudes and low altitudes. At high altitudes most of the flows are equatorward. The main differences between our 2-D and 3-D simulations is that the mid-altitude, high-latitude

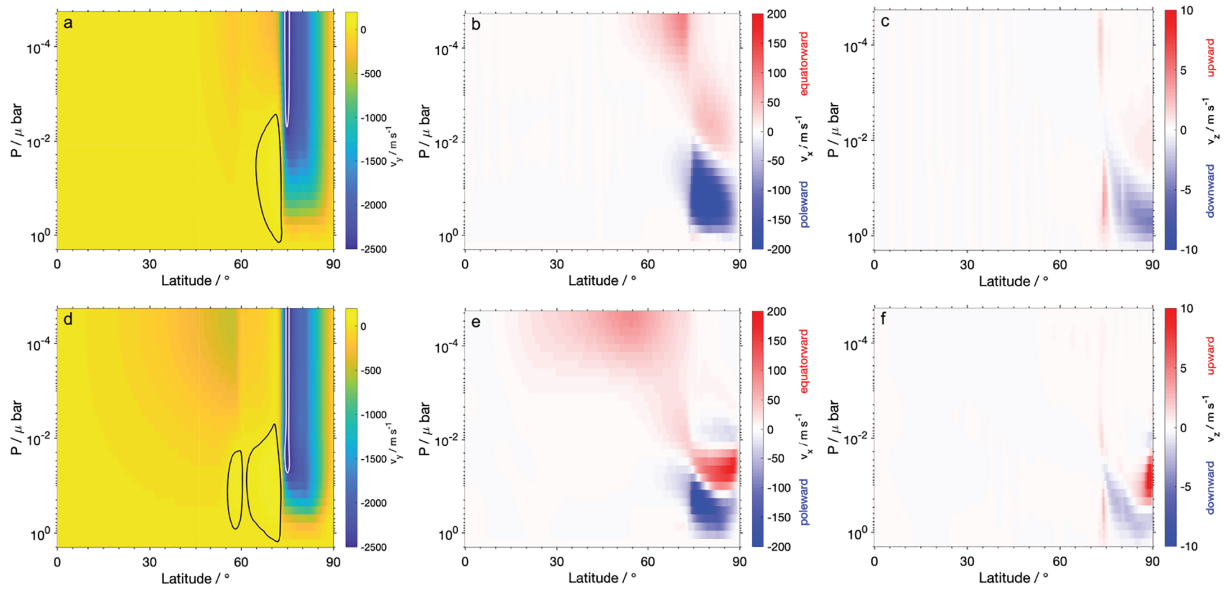

Figure 3. Two-dimensional (a–c) and 3-D (bottom row) neutral winds as a function of pressure and latitude. Panels (a) and (d) show azimuthal (east-west) velocities in the corotating frame. Black contours enclose regions of supercorotation greater than 25 m/s and white contours enclose regions of subcorotation slower than −2500 m/s. Panels (b) and (e) show meridional (north-south) velocities where equatorward (poleward) flows are positive (negative). Panels (c) and (f) show vertical velocities with upward (downward) flows being positive (negative).

equatorward 3-D flow is much stronger (∼ 2 times) than the 2-D model meaning that midaltitude winds can transport heat equatorward. Vertical winds are very similar in both simulations but the upward winds at the poles are much stronger (∼ 2.75 times) in the 3-D simulation. The faster 3-D winds lead to the averaged thermospheric angular velocity profiles shown in Figure 2. In particular, the angular velocity profile poleward of ∼85° shows that neutral winds are significantly faster than in the 2-D simulation and approach ∼0.7 Ω_J at the poles. In the 3-D simulation, eastward (corotational) fictitious (Coriolis and curvature) forces are unopposed at low altitudes beyond 75°, this accelerates the neutrals toward corotation and given that this low-altitude region has a stronger weighting in the Ω_T calculations due to its higher ionospheric conductances (see Smith & Aylward, 2009) compared to altitudes above, the integrated average Ω_T profile shows much faster winds near the poles. The large flow shears near the poles require faster vertical winds in order to maintain hydrostatic equilibrium.

Figures 4a and 4c show neutral temperature as a function of pressure and latitude for the 2-D and 3-D simulation, respectively. Figure 4b shows the 3-D temperature as a function of latitude and LT at the top pressure level of the model (0.02 nbar). The arrows indicate the direction of the horizontal winds. In addition, Figure 4d shows the vertical thermal structure for our 2-D (dashed colored lines) and 3-D (solid colored lines) simulations at various latitudes (see figure legend) compared with the Galileo probe measurements shown in black line.

From Figures 4a and 4c we see that the latitudinal and vertical structure remains relatively unchanged between our 2-D and 3-D models, that is, hot polar regions with a cold equator. The polar hot spots arise from the advection of Joule heating and ion drag energy near the model auroral zone (∼ 74°) toward the poles by strong meridional winds (e.g., Ray et al., 2015; Smith & Aylward, 2008, 2009; Tao et al., 2009; Yates et al., 2012). These rapid poleward winds also lead to upwelling of neutrals just equatorward of the auroral zone, which are cooled adiabatically creating a relatively cold spot. Adiabatic heating from downwelling at the poles and vertical advection also contribute to the polar hot spots. The cold equatorial regions result from the lack of low-latitude heat sources (in the current model setup) and the "ion drag fridge" effect discussed by Smith et al. (2007) and Smith and Aylward (2008), which gives rise to the strong low-altitude poleward flows discussed above. This effect confines heat from the magnetospheric interaction into the polar regions while essentially cooling the middle-to-low latitudes. Figure 4b shows the hot pole and cold equator. In particular, it shows the minimal effect, compared to other heat sources, of solar radiation in heating the Jovian upper thermosphere.

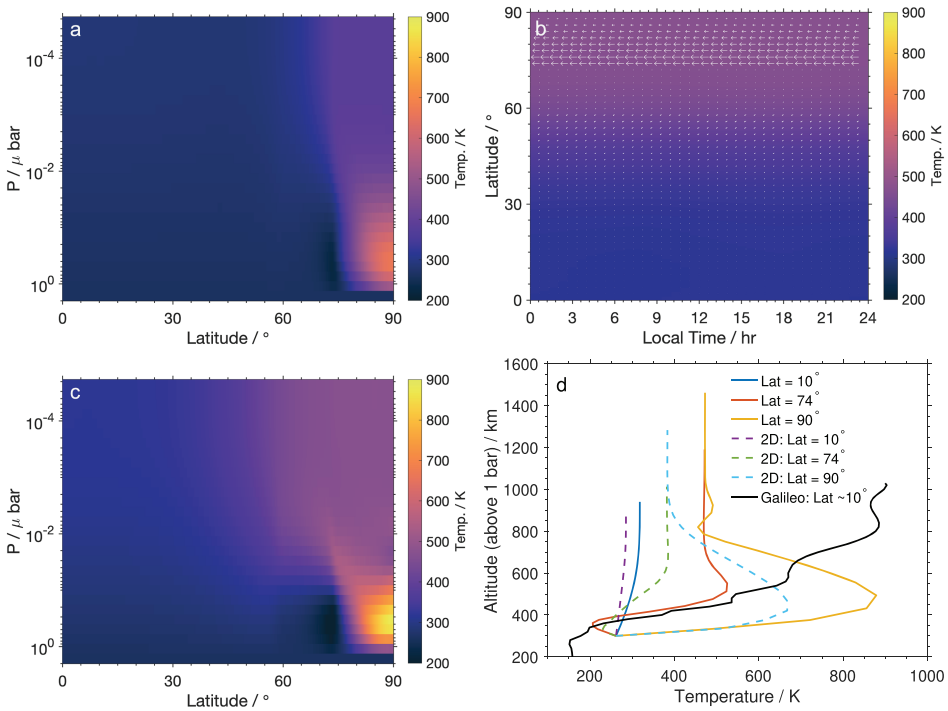

Figure 4. Two-dimensional (a) and 3-D (c) neutral temperature as a function of pressure and latitude. Panel (b) shows the 3-D temperature distribution as a function of local time and latitude. The arrows show the horizontal winds with arrow length representing their speed. Panel (d) shows the vertical thermal structure for the 2-D (dashed colored lines) and 3-D (solid colored lines) simulation at latitudes of 10°, 74°, and 90° and that measured with the Galileo probe (black line; Seiff et al., 1998).

The only difference between the two simulations is that the 3-D atmosphere is hotter than the 2-D one, at middle and high latitudes. In fact, the maximum temperature in the 3-D simulation is ~ 200 K hotter than the 2-D one (see also Figure 4d). The increase in temperature is due to a number of factors including, but not limited to, the faster wind speeds being able to redistribute more heat (including to middle and low latitudes), the increased heating rates (compared to 2-D) at polar mid-latitudes and auroral latitudes, and additional zonal advection terms—albeit this is LT dependent.

In Figure 4d we see the improvement achieved with this new 3-D simulation (compared to the 2-D one) in increasing the temperature of Jupiter's upper atmosphere. Despite this, there is still a large discrepancy at equatorial latitudes. This suggests that the current assumptions employed here and in much of the recent literature are still inadequate and that these need to be removed and/or amended to explain the observations.

3.2. Coupling Currents and Auroral Emission

The currents responsible for coupling Jupiter's atmosphere and magnetosphere can be approximated to a three-current circuit: (i) the Pedersen current in the ionosphere, (ii) the radial current in the magnetosphere, and (iii) the FAC completing the circuit. The Pedersen current is directed equatorward, and equation (2) gives the azimuthally integrated Pedersen current $I_P(\theta_i)$ (e.g., Cowley et al., 2007; Smith & Aylward, 2009) representing the total current in each hemisphere.

$$I_P(\theta_i) = 2\pi\rho_i\Sigma_P E_\theta, \tag{2}$$

where ρ_i is the perpendicular distance to the planet's magnetic/rotation axis and $E_\theta = B_i\rho_i\left(\Omega_T - \Omega_M\right)$ is the meridional electric field in the rest frame of the neutrals. B_i $(= 2B_J)$ is the magnitude of the radial ionospheric magnetic field. Radial currents are directed radially outward in the magnetodisc, and FACs connect the ionosphere to magnetosphere. FACs are responsible for angular momentum and energy transfer between the ionosphere and magnetosphere. The FAC density at the ionosphere is given by

$$j_{||i}(\theta_i) = -\frac{1}{2\pi R_i^2 \sin\theta_i}\frac{dI_P}{d\theta_i}. \tag{3}$$

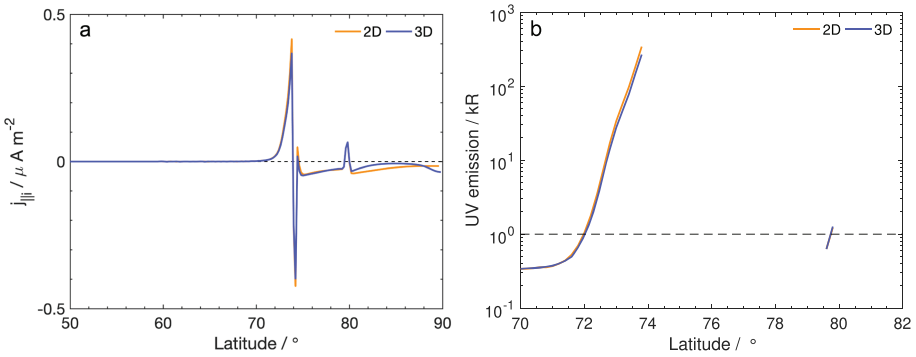

Figure 5. Ionospheric field-aligned current density (a) and auroral ultraviolet (UV) emission (b) is shown as a function of latitude. 2-D and 3-D current/emission are represented by the orange and blue lines respectively. The dashed line in (b) shows the limit of detectability of the Hubble Space Telescope.

Figure 5a compares the FAC density profiles in the 3-D simulation (blue line) with the 2-D simulation (orange line). Figure 5b shows the corresponding brightness of the UV auroral emission associated with these FACs. Auroral emissions are calculated from the precipitating electron energy flux assuming that 1 mW/m^{-2} = 10 kR as described by Yates et al., 2014 (2014; based on the works of Cowley et al., 2007; Knight, 1973; Lundin & Sandahl, 1978) in order to allow for comparison. However, it is worth noting that recent Juno observations (Ebert et al., 2019) have found that the above relationship between downward energy flux and auroral emission is not always true across the auroral region and would require a deeper understanding of Jupiter electron acceleration region.

The FAC density profiles show regions of strong upward FACs maximizing at 74°. Upward FACs mean downward propagating electrons, which collide with atmospheric neutrals and result in UV emission. These upward FACs therefore correspond to the large peaks in auroral emission shown in Figure 5b, which represent the main auroral oval in our coupled MIT model. The regions of upward FAC are immediately followed by strong downward FACs indicating the return current. With the present model, no emission is expected in this region. Even further poleward, our model has another region of upward FACs and corresponding UV emission but with much smaller magnitude than that of the main oval. This region corresponds to the boundary between our model's outer magnetosphere (or cushion region) and the polar cap (open field region). The magnetospheric flows in this region are not well constrained by observations so the currents and emissions are susceptible to the values we prescribe for plasma flow and ionospheric conductances here. The maximum upward FAC in the 3-D simulation is ∼ 90% that of the 2-D simulation. This difference is caused by the shear between the neutral and plasma angular velocities being larger around ∼74° latitude in the 2-D simulation than in the 3-D one because of the 3-D neutral winds subcorotating to a larger degree in this region (see Figure 2). The corresponding maximum auroral emissions amount to UV brightnesses of ∼270 kR for our 3-D simulation and ∼340 kR for the 2-D one with total integrated powers of ∼ 2 and ∼ 2.5 TW respectively. These emissions are of similar order-of-magnitude to observations and the integrated powers are comparable to recent observations taken using the Hubble Space Telescope (e.g., 1–3 TW in Grodent et al., 2018), the Hisaki space telescope (e.g., ∼1.3 up to ∼11 TW Tao et al., 2018), and the UV spectrograph instrument (Gladstone et al., 2017) onboard the Juno spacecraft (e.g., 2–3 TW in Gladstone et al., 2017).

3.3. Atmospheric Energetics

We also examine the energy transferred from Jupiter's deep rotation to its upper atmosphere and magnetosphere. The power per unit area available due to Jupiter's rotation is given by P; this can be subdivided into the power used to accelerate subcorotating plasma within Jupiter's magnetosphere P_{M} and the power dissipated within Jupiter's upper atmosphere consisting of Joule heating P_{JH} and ion drag P_{ID}.

$$P = \Omega_J \tau,$$

$$P_{\mathrm{JH}} = (\Omega_T - \Omega_M)\tau, \tag{4}$$

$$P_{\mathrm{ID}} = (\Omega_J - \Omega_T)\tau, \tag{5}$$

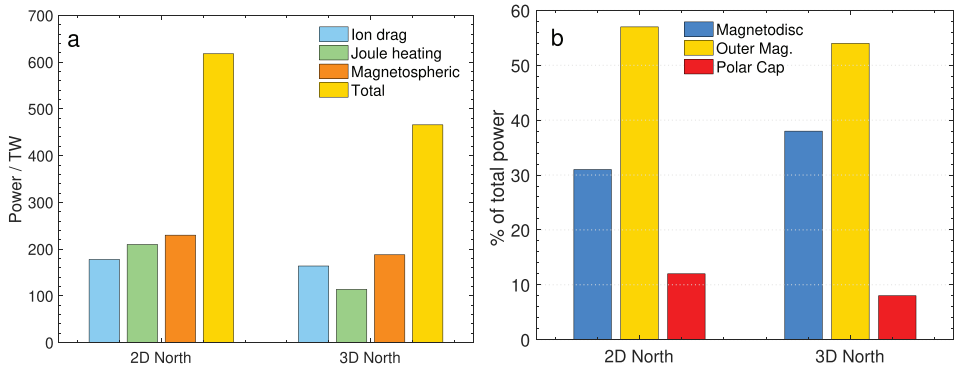

Figure 6. Panel (a) shows integrated ion drag (light blue), Joule heating (light green), magnetospheric (orange), and total (gold) power per hemisphere for the 2-D model and the northern hemisphere of the 3-D model. Panel (b) shows the fraction of total integrated power mapping to the magnetodisc (55.4–74.2° latitude shown in blue), outer magnetosphere (74.2–79.8° latitude shown in gold), and polar cap (79.8–90° latitude shown in red) regions of the magnetosphere.

$$P_M = \Omega_M \tau, \tag{6}$$

where $\tau = \rho_i i_P B_i$ is the torque exerted by the $\mathbf{J} \times \mathbf{B}$ force per unit area of the ionosphere; $i_P = I_P/(2\pi\rho_i)$ and is the Pedersen current density.

Figure 6a shows the integrated ion drag (light blue), Joule heating (light green), magnetospheric (orange), and total (gold) power per hemisphere for the 2-D simulation (northern hemisphere) along with the northern hemisphere in the 3-D simulation. Immediately obvious is that the powers in the 2-D simulation are larger than each 3-D hemisphere. Ion drag, Joule heating, and magnetospheric powers are respectively ∼1.06, ∼1.8, and ∼1.2 times larger in the 2-D simulation than the 3-D one. The differences between the 3-D and 2-D simulations are primarily due to the difference in neutral angular velocity between the two. As shown in Figures 2, 3a, and 3d, the neutral winds between 73° and 86° latitude subcorotate to a much larger degree in the 3-D simulation leading to smaller Pedersen currents (and torques) in the ionosphere. This large region of subcorotating neutral flow maps to regions of the magnetosphere whose flows are prescribed in our model (for details see section 2.5 or Yates et al. (2012)) suggesting that these changes are purely due to atmospheric effects and the added momentum and energy terms in the 3-D simulation. Figure 6b shows the fraction of power in atmospheric regions mapping to the magnetodisc (55.4–74.2° latitude shown in blue), outer magnetosphere (74.2–79.8° latitude shown in gold), and polar cap (79.8–90° latitude shown in red). The fraction of power used in the outer magnetosphere is similar for both 2-D and 3-D simulations. The differences lie in the power used in the magnetodisc and polar cap regions where the 3-D simulation uses ∼7% more power in the magnetodisc and ∼5% less power in the polar cap. From Figure 6b we see that approximately 60–70% of power extracted from Jupiter's rotation is consumed within atmospheric regions where we prescribe the plasma flows. In order to understand how Jupiter's atmosphere is heated we must gain better understanding of the plasma flows in the high-latitude ionosphere, which map to the distant magnetosphere.

4. Discussion

4.1. Comparison With Observations

4.1.1. Neutral Temperatures

There are many in situ observations of Jupiter's magnetosphere. On the other hand, Jupiter's atmosphere has only one set of in situ observations by NASA's Galileo Probe (see black line in Figure 4d and/or Seiff et al., 1998). All other observations of Jupiter's atmosphere are remote (space- or Earth-based telescopes). Temperatures of Jupiter's upper atmosphere can be inferred remotely from auroral observations at infrared (IR) and ultraviolet (UV) wavelengths (e.g., Adriani et al., 2017; Johnson et al., 2018; Kita et al., 2018; Lam et al., 1997; Lystrup et al., 2008; Migliorini et al., 2019; Moore et al., 2017; Raynaud et al., 2004; Stallard et al., 2002; Yelle et al., 1996). Using IR emission from the ionospheric H_3^+ ion, Jupiter's thermospheric temperature is observed to range from ∼ 400 K at 300 km (above the 1-bar level) and increasing to between ∼ 900 and

$\sim$ 1400 K at altitudes $\geq$ 700 km, with larger temperatures located at higher latitudes (e.g., Johnson et al., 2018; Migliorini et al., 2019; Moore et al., 2017).

Comparison of our model neutral temperatures to those observed can be split into two regions:

1. The polar thermosphere ($\geq$ 74°): Here, our model achieved its maximum temperature of 878 K at low polar altitudes ($\sim$ 500 km). Our model temperatures then decrease with increasing altitude to $\sim$ 450 K. This is contrary to expectations and available observations. This temperature inversion is likely caused by the lack of (or weak) energy sources at high altitudes within our model. The heat in this region is transported toward the equator by the high-altitude equatorward winds. The higher model temperatures in this polar region are comparable to the lower limit of the observed high-latitude temperatures but at higher altitudes our model temperatures are at most 50% of those observed.
2. The mid- to low-latitude thermosphere (<74°): The high-altitude temperature maximums vary from $\sim$ 320 K at the equator to $\sim$ 480 K at 70°. These maximums are approximately a factor of 2 times smaller than the mid- to low-latitude temperatures derived by O'Donoghue et al. (2016) at altitudes between 600 and 1,000 *km*. At low altitudes these temperatures have an average of $\sim$ 290 K with a base of 260 K at the lower boundary (equivalent to 300 km above the 1-bar level). These temperatures are ~100–200 K smaller than those determined at 300 km by Migliorini et al. (2019). Compared to the Galileo Probe measurements, our equatorial model temperatures are similar only at altitudes lower than 400 km; at higher altitudes our equatorial temperatures are ~100–600 K smaller than measured.

The differences between the model temperatures and observations act to highlight that there is still much work to be done in being able to reproduce the observations. Other sources of heat, such as wave heating (Müller-Wodarg et al., 2019; Tao et al., 2009), need to be included in the model as well as a better understanding of the distant magnetospheric plasma flows.

4.1.2. Neutral Winds

In addition to estimating thermospheric neutral temperatures, Jupiter's auroral IR emission can be used to determine the line-of-sight velocity of H_3^+ ions (Jupiter's main ionospheric constituent) using the Doppler shift technique (e.g., Chaufray et al., 2011; Johnson et al., 2017; Stallard et al., 2001). The works of Stallard and Johnson find regions where the ionosphere is supercorotating between $\sim$ 0.5 and 1 km/s and regions where it is subcorotating between $\sim$ 1 and 2 km/s. Chaufray et al. (2011), however, only found ionospheric winds subcorotating at $\sim$ 3 km/s. Additionally, Chaufray et al. estimated neutral wind velocities in Jupiter's thermosphere using IR emissions from H_2; these were found to be of order $\sim$ 1 km/s, suggesting that the neutral thermosphere rotates faster than the ionosphere. The authors do note that more simultaneous neutral and ion wind measurements are needed to fully understand the system.

Our new 3-D model obtains both supercorotating and subcorotating neutral winds and ion/plasma angular velocities. The neutral zonal winds achieve velocities between $\sim$ 0.25 (supercorotating) and $\sim$ −2.7 km/s (subcorotating). We do not calculate ionospheric ion winds using the ion momentum equation but instead calculate the plasma angular velocity (using the Hill-Pontius equation described in section 2.4) within the magnetosphere and assume that the ionospheric plasma angular velocity is the same. In order to use this method, the magnetosphere interacts with an "effective" neutral thermosphere and therefore an effective neutral angular velocity Ω_T which is dependent on both the zonal and meridional neutral winds. The plasma angular velocity up to the auroral region ~74° tracks Ω_T very well albeit being a little smaller. Our model neutral and plasma velocities are comparable to those in the above observational studies up to the auroral oval region. Poleward of this region, our plasma flows are prescribed to rotate at a small fraction of Jupiter's rotation velocity as is shown in Figure 2. The polar region neutral flows are strongly influenced by these prescribed flows and should be interpreted with a degree of skepticism. However, we note that the line-of-sight velocity of H_3^+ ions observed by Johnson et al. (2017) in their UV-dark region shows flows that are near stationary ($<$ 20% of Ω_J). If we assume that the UV-dark region applies to a "polar cap"-type region, then these observations add credence to our use of small plasma velocities. Nevertheless, more observations of Jupiter's polar ionosphere and outer magnetosphere are needed to further constrain the ionospheric flows and NASA's Juno mission (Bolton et al., 2017) can shed some light on this poorly understood region.

4.2. Comparison With Other Jovian 3-D Models

There are a few 3-D Jovian upper atmospheric models that investigate Jupiter's MIT coupling (JIM and JTGCM). These models do not self-consistently couple the upper atmosphere to the magnetosphere but

instead impose electric and magnetic fields, and MI coupling parameterizations onto the atmospheric model. They do however include detailed atmospheric chemistry and therefore include a somewhat realistic ionosphere. In contrast, the new model described in section 2 includes MIT coupling self-consistently in addition to solving the atmospheric neutral momentum and energy equations. It, however, includes only a simplified conductivity parameterization representing Jupiter's ionosphere. The differences in the ionospheric components of these models result in different values of Pedersen conductances, which is important in MIT coupling (e.g., Ray et al., 2015). The JIM (Millward et al., 2002) model conductances are comparable (1–3 times) to those used in this study but conductances in JTGCM (Bougher et al., 2005) are $\sim$ 10 times higher than those employed here. Furthermore, we assume that our magnetic field model is rotationally aligned and axisymmetric, contrary to the magnetic field models employed in JIM (offset tilted dipole (Acuna et al., 1983)) and JTGCM (VIP4; Connerney et al., 1998). We therefore perform only simple comparisons between this new model and previous Jovian 3-D MIT models. We note that this new model, as described herein, is midway in its development to include self-consistent 3-D MIT coupling.

With regard to neutral temperature, our model is generally colder than both JIM and JTGCM with the exception being in the low-altitude polar regions where our models have comparable temperatures. JIM's atmospheric temperature increases from 400 K at the models lower boundary to 1200 K at its upper boundary and is heated primarily by Joule heating and auroral particle precipitation. It is worth noting that while the JIM model did reach a quasi-dynamical equilibrium state, it did not achieve thermal equilibrium during its model runs. JTGCM includes ion drag, particle precipitation, and Joule heating, but their Joule heating parameterization requires being downscaled to 15% in order to reproduce equatorial temperature profiles comparable to those observed by the Galileo Probe. JTGCM's high-latitude temperatures reach $\sim$ 1100 K in the southern polar region and $\sim$ 900 K in the northern due to asymmetries in the VIP4 magnetic field model.

Zonal thermospheric neutral velocities were found to be of order $\sim$ 0.5 km/s in the JIM model (e.g., Millward et al., 2005) compared to $\sim$ 1.6 km/s and $\sim$ 0.6 km/s respectively in JTGCMs southern and northern auroral ovals (e.g., Majeed et al., 2016). These result from ion winds of $\sim$ 1 km/s in JIM and $\sim$ 3.5 km/s in JTGCM (note that ion winds are imposed in JTGCM). The zonal winds in our new model are typically stronger (more subcorotating) than both JIM and JTGCM, reaching subcorotating values of $\sim$ 2.7 km/s. Our model also includes a region equatorward of the auroral oval where the neutral atmosphere supercorotates with speeds up to $\sim$ 0.25 km/s resulting from the Coriolis force and strong ($\sim$ 0.2 – −0.3 km/s) low-altitude poleward winds. Above the peak conducting region, our meridional flows switch to being equatoward and with similar speed. These equatorward flows slow down to only a few meters per second at the equator. The meridional winds in JTGCM and JIM are stronger than in the model presented herein and reach poleward speeds up to $\sim$ 0.6 km/s and equatoward speeds of $\sim$ 0.25 km/s. As discussed above, JTGCM employs the VIP4 magnetic field model, which causes considerable asymmetry in heating and neutral flows. As such, JTGCM also obtains strong ($\sim$ 0.1 – −0.2 km/s) equatorward flows even at low southern latitudes, which allows for the redistribution of heat from the auroral region.

5. Summary and Conclusions

Jupiter's upper atmosphere is $\sim$ 700 K hotter than predicted based on solar EUV heating alone. The interaction with Jupiter's strong and dynamic magnetosphere is thought to play a vital role in heating its upper atmosphere to its observed temperatures. However, to date no coupled MIT model has been able to self-consistently reproduce Jupiter's thermospheric temperatures without imposing particular plasma flows, large Pedersen conductances inconsistent with modeling/predictions, and/or including a low-latitude heat source such as acoustic wave breaking or small-scale Joule heating generated by fluctuating electric fields. We present a new model of Jupiter's MIT coupled system that couples a three-dimensional atmospheric GCM to an axisymmetric magnetosphere model. This new model is an intermediate step toward the development of a self-consistently coupled 3-D atmosphere-magnetosphere model. We compare this new model to its two-dimensional predecessor, available observations and other 3-D Jovian upper atmosphere models.

Compared to the 2-D simulations of Yates et al. (2014), the new model has a mean temperature that is ~60 K hotter, with a maximum temperature that is ~200 K hotter in the polar regions. Zonal and poleward neutral winds were found to be comparable in both simulations while the equatorward winds are twice as strong (~190 m/s) in the new 3-D simulation resulting in more energy transport from high to low latitudes. Three-dimensional vertical winds were also found to be 2–3 times stronger in the upward direction and half

as strong in the downward direction. The velocity shear between the neutrals and plasma is larger in the 2-D simulation between 74–86° leading to larger MI coupling currents, powers, and UV emission. Our 3-D model is still in development and is not yet fully comparable to the other 3-D Jovian thermosphere models available. However, our model is converging toward the results found in the JIM and JTGCM models and unlike these models it also includes self-consistent coupling between the ionosphere and magnetosphere. Our model also compares reasonably well with some ionospheric wind observations and its predicted total UV power is of the same order of magnitude as those determined from Hubble Space Telescope observations. The neutral temperatures in the auroral and polar regions are comparable to the lower range of observed temperatures, while the models equatorial temperatures are still a few hundreds of kelvins colder than observed.

The axisymmetric rotationally aligned magnetosphere model that we employ in this study results in a small (few degrees latitude) circular region of interaction between Jupiter's magnetosphere and atmosphere centered on 74° latitude. In actuality, Jupiter's magnetic field is tilted with respect to its rotation axis and has very complex structure (e.g., Connerney et al., 2018). Furthermore, observations of Jupiter's auroral emission—a "visible" manifestation of the MI interaction—show that this interaction region is anything but small and circular; in fact, it is highly asymmetric within and between each hemisphere (e.g., Connerney et al., 2017). Such a complex asymmetric interaction region would lead to different neutral flow and heating structures which cannot be simulated with the current model setup. The JIM and JTGCM models, while not self-consistently coupling the atmosphere and magnetosphere, do employ more realistic magnetic field models at the planet, which is one of the main reasons that their findings are different from those presented above. The next step in the development of the presented model is to include a more realistic magnetic field model (e.g., Connerney et al., 2018) including realistic mapping from the magnetosphere to the ionosphere and LT variation, a more detailed ionosphere model (e.g., Blelly et al., 2019), and parameterizations allowing for the incorporation of atmospheric waves (e.g., Tao et al., 2009; Müller-Wodarg et al., 2019). This model will be the most realistic three-dimensional representation of Jupiter's coupled magnetosphere-atmosphere system.

Acknowledgments
J. N. Y. was supported by a European Space Agency research fellowship. L. C. R. acknowledges the STFC Consolidated GrantST/R000816/1. N. A. was supported by the U.K. STFC Consolidated Grant (UCL/MSSL Solar and Planetary Physics, ST/N000722/1). The authors acknowledge the International Space Science Institute (ISSI) for their support of the "Coordinated Numerical Modeling of the Global Jovian and Saturnian Systems" team. The Galileo Probe observations are available from the Planetary Data System (http://pds.nasa.gov/) and are peer reviewed. The simulation output used in this study is available at https://figshare.com/s/9c49feccbc77634b83cd. The authors would like to thank both referees for their useful suggestions.

References

Achilleos, N., Miller, S., Prangé, R., Millward, G., & Dougherty, M. K. (2001). A dynamical model of Jupiter's auroral electrojet. *New Journal of Physics*, *3*, 3. https//doi.org/10.1088/1367-2630/3/1/303

Achilleos, N., Miller, S., Tennyson, J., Aylward, A. D., Mueller-Wodarg, I., & Rees, D. (1998). JIM: A time-dependent, three-dimensional model of Jupiter's thermosphere and ionosphere. *Journal of Geophysical Research*, *103*, 20,089–20,112. https//doi.org/10.1029/98JE00947

Acuna, M. H., Behannon, K. W., & Connerney, J. E. P. (1983). *Jupiter's magnetic field and magnetosphere* (pp. 1–50). Cambridge, New York: Cambridge University Press.

Adriani, A., Mura, A., Moriconi, M. L., Dinelli, B. M., Fabiano, F., Altieri, F., et al. (2017). Preliminary JIRAM results from Juno polar observations: 2. Analysis of the Jupiter southern H_3^+ emissions and comparison with the north aurora. *Geophysical Research Letters*, *44*, 4633–4640. https//doi.org/10.1002/2017GL072905

Blelly, P.-L., Marchaudon, A., Indurain, M., Witasse, O., Amaya, J., Chide, B., et al. (2019). Transplanet: A web service dedicated to modeling of planetary ionospheres. *Planetary and Space Science*, *169*, 35–44. https//doi.org/10.1016/j.pss.2019.02.008

Bolton, S. J., Lunine, J., Stevenson, D., Connerney, J. E. P., Levin, S., Owen, T. C., et al. (2017). The Juno mission. *Space Science Reviews*, *213*, 5–37. https//doi.org/10.1007/s11214-017-0429-6

Bougher, S. W., Waite, J. H., Majeed, T., & Gladstone, G. R. (2005). Jupiter Thermospheric General Circulation Model (JTGCM): Global structure and dynamics driven by auroral and Joule heating. *Journal of Geophysical Research*, *110*, E04008. https//doi.org/10.1029/2003JE002230

Chaufray, J.-Y., Greathouse, T. K., Gladstone, G. R., Waite, J. H., Maillard, J.-P., Majeed, T., et al. (2011). Spectro-imaging observations of Jupiters 2 μm auroral emission. II: Thermospheric winds. *Icarus*, *211*, 1233–1241. https//doi.org/10.1016/j.icarus.2010.11.021

Connerney, J. E. P., Acuña, M. H., Ness, N. F., & Satoh, T. (1998). New models of Jupiter's magnetic field constrained by the Io flux tube footprint. *Journal of Geophysical Research*, *103*, 11,929–11,940. https//doi.org/10.1029/97JA03726

Connerney, J. E. P., Adriani, A., Allegrini, F., Bagenal, F., Bolton, S. J., Bonfond, B., et al. (2017). Jupiter's magnetosphere and aurorae observed by the Juno spacecraft during its first polar orbits. *Science*, *356*, 826–832. https//doi.org/10.1126/science.aam5928

Connerney, J. E. P., Kotsiaros, S., Oliversen, R. J., Espley, J. R., Joergensen, J. L., Joergensen, P. S., et al. (2018). A new model of Jupiter's magnetic field from Juno's first nine orbits. *Geophysical Research Letters*, *45*, 2590–2596. https//doi.org/10.1002/2018GL077312

Cowley, S. W. H., Alexeev, I. I., Belenkaya, E. S., Bunce, E. J., Cottis, C. E., Kalegaev, V. V., et al. (2005). A simple axisymmetric model of magnetosphere-ionosphere coupling currents in Jupiter's polar ionosphere. *Journal of Geophysical Research*, *110*, 11,209–11,226. https//doi.org/10.1029/2005JA011237

Cowley, S. W. H., Nichols, J. D., & Andrews, D. J. (2007). Modulation of Jupiter's plasma flow, polar currents, and auroral precipitation by solar wind-induced compressions and expansions of the magnetosphere: A simple theoretical model. *Annales Geophysicae*, *25*, 1433–1463.

Ebert, R. W., Greathouse, T. K., Clark, G., Allegrini, F., Bagenal, F., Bolton, S. J., et al. (2019). Comparing electron energetics and UV brightness in Jupiter's Northern Polar Region during Juno Perijove 5. *Geophysical Research Letters*, *46*, 19–27. https//doi.org/10.1029/2018GL081129

Gladstone, G. R., Persyn, S. C., Eterno, J. S., Walther, B. C., Slater, D. C., Davis, M. W., et al. (2017). The ultraviolet spectrograph on NASA's Juno mission. *Space Science Reviews*, *213*, 447–473. https//doi.org/10.1007/s11214-014-0040-z

Gladstone, G. R., Versteeg, M. H., Greathouse, T. K., Hue, V., Davis, M. W., Gérard, J.-C., et al. (2017). Juno-UVS approach observations of Jupiter's auroras. *Geophysical Research Letters*, *44*, 7668–7675. https//doi.org/10.1002/2017GL073377

Grodent, D., Bonfond, B., Yao, Z., Gérard, J.-C., Radioti, A., Dumont, M., et al. (2018). Jupiter's aurora observed with HST during Juno Orbits 3 to 7. *Journal of Geophysical Research: Space Physics*, *123*, 3299–3319. https//doi.org/10.1002/2017JA025046

Grodent, D., Waite, J. H., & Gérard, J.-C. (2001). A self-consistent model of the Jovian auroral thermal structure. *Journal of Geophysical Research*, *106*, 12,933–12,952. https//doi.org/10.1029/2000JA900129

Hickey, M. P., Walterscheid, R. L., & Schubert, G. (2000). Gravity wave heating and cooling in Jupiter's thermosphere. *Icarus*, *148*, 266–281. https//doi.org/10.1006/icar.2000.6472

Hill, T. W. (1979). Inertial limit on corotation. *Journal of Geophysical Research*, *84*, 6554–6558. https//doi.org/10.1029/JA084iA11p06554

Hill, T. W. (1980). Corotation lag in Jupiter's magnetosphere—Comparison of observation and theory. *Science*, *207*, 301–302. https//doi.org/10.1126/science.207.4428.301

Isbell, J., Dessler, A. J., & Waite, J. H. (1984). Magnetospheric energization by interaction between planetary spin and the solar wind. *Journal of Geophysical Research*, *89*, 10,716–10,722. https//doi.org/10.1029/JA089iA12p10716

Johnson, R. E., Melin, H., Stallard, T. S., Tao, C., Nichols, J. D., & Chowdhury, M. N. (2018). Mapping h3+ temperatures in Jupiter's northern auroral ionosphere using VLT-CRIRES. *Journal of Geophysical Research: Space Physics*, *123*, 5990–6008. https//doi.org/10.1029/2018JA025511

Johnson, R. E., Stallard, T. S., Melin, H., Nichols, J. D., & Cowley, StanW. H. (2017). Jupiter's polar ionospheric flows: High resolution mapping of spectral intensity and line-of-sight velocity of h3+ ions. *Journal of Geophysical Research: Space Physics*, *122*, 7599–7618. https//doi.org/10.1002/2017JA024176

Khurana, K. K. (2001). Influence of solar wind on Jupiter's magnetosphere deduced from currents in the equatorial plane. *Journal of Geophysical Research*, *106*, 25,999–26,016. https//doi.org/10.1029/2000JA000352

Kita, H., Fujisawa, S., Tao, C., Kagitani, M., Sakanoi, T., & Kasaba, Y. (2018). Horizontal and vertical structures of Jovian infrared aurora: Observation using Subaru IRCS with adaptive optics. *Icarus*, *313*, 93–106. https//doi.org/10.1016/j.icarus.2018.05.002

Knight, S. (1973). Parallel electric fields. *Planetary and Space Science*, *21*, 741–750. https//doi.org/10.1016/0032-0633(73)90093-7

Lam, H. A., Achilleos, N., Miller, S., Tennyson, J., Trafton, L. M., Geballe, T. R., & Ballester, G. E. (1997). A baseline spectroscopic study of the infrared auroras of Jupiter. *Icarus*, *127*, 379–393. https//doi.org/10.1006/icar.1997.5698

Lundin, R., & Sandahl, I. (1978). Some characteristics of the parallel electric field acceleration of electrons over discrete auroral arcs as observed from two rocket flights. In T. Halvorsen & B. Battrick (Eds.), *European sounding rocket, balloon and related research, with emphasis on experiments at high latitudes* (Vol. 135, pp. 125–136): ESA Special Publication.

Lystrup, M. B., Miller, S., Dello Russo, N., Vervack, R. J., & Stallard, T. (2008). First vertical ion density profile in Jupiter's auroral atmosphere: Direct observations using the Keck II telescope. *Astrophysical Journal*, *677*, 790–797. https//doi.org/10.1086/529509

Majeed, T., Bougher, S. W., Ridley, A. J., Waite, J. H., Gladstone, G. R., & Bell, J. M. (2016). Global response of the upper thermospheric winds to large ion drifts in the Jovian ovals. *Journal of Geophysical Research: Space Physics*, *121*, 4647–4667. https//doi.org/10.1002/2015JA021328

Majeed, T., Waite, J. H., Bougher, S. W., & Gladstone, G. R. (2005). Processes of equatorial thermal structure at Jupiter: An analysis of the Galileo temperature profile with a three-dimensional model. *Journal of Geophysical Research*, *110*, E12007. https//doi.org/10.1029/2004JE002351

Majeed, T., Waite, J. H., Bougher, S. W., & Gladstone, G. R. (2009). Processes of auroral thermal structure at Jupiter: Analysis of multispectral temperature observations with the Jupiter Thermosphere General Circulation Model. *Journal of Geophysical Research*, *114*, E07005. https//doi.org/10.1029/2008JE003194

Matcheva, K. I., & Strobel, D. F. (1999). Heating of Jupiter's thermosphere by dissipation of gravity waves due to molecular viscosity and heat conduction. *Icarus*, *140*, 328–340. https//doi.org/10.1006/icar.1999.6151

Migliorini, A., Dinelli, B. M., Moriconi, M. L., Altieri, F., Adriani, A., Mura, A., et al. (2019). H_3^+ characteristics in the Jupiter atmosphere as observed at limb with Juno/JIRAM. *Icarus*, *329*, 132–139. https//doi.org/10.1016/j.icarus.2019.04.003

Miller, S., Achilleos, N., Ballester, G. E., Geballe, T. R., Joseph, R. D., Prangé, R., et al. (2000). The role of H_3^+ in planetary atmospheres, *Astronomy, physics and chemistry of* H_3^+, *Royal Society of London Philosophical Transactions Series A* (Vol. 358, pp. 2485). England: the Royal Society. https//doi.org/10.1098/rsta.2000.0662

Millward, G., Miller, S., Stallard, T., Achilleos, N., & Aylward, A. D. (2005). On the dynamics of the Jovian ionosphere and thermosphere.. IV. Ion-neutral coupling. *Icarus*, *173*, 200–211. https//doi.org/10.1016/j.icarus.2004.07.027

Millward, G., Miller, S., Stallard, T., Aylward, A. D., & Achilleos, N. (2002). On the dynamics of the Jovian ionosphere and thermosphere III. The modelling of auroral conductivity. *Icarus*, *160*, 95–107. https//doi.org/10.1006/icar.2002.6951

Moore, L., O'Donoghue, J., Melin, H., Stallard, T., Tao, C., Zieger, B., et al. (2017). Variability of Jupiter's IR H_3^+ aurorae during Juno approach. *Geophysical Research Letters*, *44*, 4513–4522. https//doi.org/10.1002/2017GL073156

Müller-Wodarg, I. C. F., Koskinen, T. T., Moore, L., Serigano, J., Yelle, R. V., Hörst, S., et al. (2019). Atmospheric waves and their possible effect on the thermal structure of Saturn's thermosphere. *Geophysical Research Letters*, *46*, 2372–2380. https//doi.org/10.1029/2018GL081124

Müller-Wodarg, I. C. F., Mendillo, M., Yelle, R. V., & Aylward, A. D. (2006). A global circulation model of Saturn's thermosphere. *Planetary and Space Science*, *180*, 147–160. https//doi.org/10.1016/j.icarus.2005.09.002

Nichols, J. D. (2011). Magnetosphere-ionosphere coupling in Jupiter's middle magnetosphere: Computations including a self-consistent current sheet magnetic field model. *Journal of Geophysical Research*, *116*, A10232. https//doi.org/10.1029/2011JA016922

Nichols, J., & Cowley, S. (2004). Magnetosphere-ionosphere coupling currents in Jupiter's middle magnetosphere: Effect of precipitation-induced enhancement of the ionospheric Pedersen conductivity. *Annales Geophysicae*, *22*, 1799–1827.

O'Donoghue, J., Moore, L., Stallard, T. S., & Melin, H. (2016). Heating of Jupiter's upper atmosphere above the Great Red Spot. *Nature*, *536*(7615), 190–192. https//doi.org/10.1038/nature18940

Pontius, D. H. (1997). Radial mass transport and rotational dynamics. *Journal of Geophysical Research*, *102*, 7137–7150. https//doi.org/10.1029/97JA00289

Pontius, D. H. Jr., & Hill, T. W. (1982). Departure from corotation of the Io plasma torus—Local plasma production. *Geophysical Research Letters*, *9*, 1321–1324. https//doi.org/10.1029/GL009i012p01321

Ray, L. C., Achilleos, N. A., Vogt, M. F., & Yates, J. N. (2014). Local time variations in Jupiter's magnetosphere-ionosphere coupling system. *Journal of Geophysical Research: Space Physics*, *119*, 4740–4751. https//doi.org/10.1002/2014JA019941

Ray, L. C., Achilleos, N. A., & Yates, J. N. (2015). The effect of including field-aligned potentials in the coupling between Jupiter's thermosphere, ionosphere, and magnetosphere. *Journal of Geophysical Research: Space Physics*, *120*, 6987–7005. https//doi.org/10.1002/2015JA021319

Raynaud, E., Lellouch, E., Maillard, J.-P., Gladstone, G. R., Waite, J. H., Bézard, B., et al. (2004). Spectro-imaging observations of Jupiter's 2-μm auroral emission. I. H_3^+ distribution and temperature. *Icarus*, *171*, 133–152. https//doi.org/10.1016/j.icarus.2004.04.020

Schubert, G., Hickey, M. P., & Walterscheid, R. L. (2003). Heating of Jupiter's thermosphere by the dissipation of upward propagating acoustic waves. *Icarus*, *163*, 398–413. https//doi.org/10.1016/S0019-1035(03)00078-2

Seiff, A., Kirk, D. B., Knight, T. C. D., Young, R. E., Mihalov, J. D., Young, L. A., et al. (1998). Thermal structure of Jupiter's atmosphere near the edge of a 5-μm hot spot in the north equatorial belt. *Journal of Geophysical Research*, *103*, 22,857–22,890. https//doi.org/10.1029/98JE01766

Smith, C. G. A., & Aylward, A. D. (2008). Coupled rotational dynamics of Saturn's thermosphere and magnetosphere: A thermospheric modelling study. *Annales Geophysicae*, *26*, 1007–1027.

Smith, C. G. A., & Aylward, A. D. (2009). Coupled rotational dynamics of Jupiter's thermosphere and magnetosphere. *Annales Geophysicae*, *27*, 199–230.

Smith, C. G. A., Aylward, A. D., Millward, G. H., Miller, S., & Moore, L. E. (2007). An unexpected cooling effect in Saturn's upper atmosphere. *Nature*, *445*, 399–401. https//doi.org/10.1038/nature05518

Smith, C. G. A., Miller, S., & Aylward, A. D. (2005). Magnetospheric energy inputs into the upper atmospheres of the giant planets. *Annales Geophysicae*, *23*, 1943–1947.

Stallard, T., Miller, S., Millward, G., & Joseph, R. D. (2001). On the Dynamics of the Jovian ionosphere and thermosphere. I. The measurement of ion winds. *Icarus*, *154*, 475–491. https//doi.org/10.1006/icar.2001.6681

Stallard, T., Miller, S., Millward, G., & Joseph, R. D. (2002). On the dynamics of the Jovian ionosphere and thermosphere. II. The measurement of H_3^+ vibrational temperature, column density, and total emission. *Icarus*, *156*, 498–514. https//doi.org/10.1006/icar.2001.6793

Strobel, D. F., & Smith, G. R. (1973). On the temperature of the Jovian thermosphere. *Journal of Atmospheric Sciences*, *30*, 718–725. https//doi.org/10.1175/1520-0469(1973)030<0718:OTTOTJ>2.0.CO;2

Tao, C., Fujiwara, H., & Kasaba, Y. (2009). Neutral wind control of the Jovian magnetosphere-ionosphere current system. *Journal of Geophysical Research*, *114*, 8307–8323. https//doi.org/10.1029/2008JA013966

Tao, C., Fujiwara, H., & Kasaba, Y. (2010). Jovian magnetosphere-ionosphere current system characterized by diurnal variation of ionospheric conductance. *Planetary and Space Science*, *58*, 351–364. https//doi.org/10.1016/j.pss.2009.10.005

Tao, C., Kimura, T., Tsuchiya, F., Muirakami, G., Yoshioka, K., Yamazaki, A., et al. (2018). Variation of Jupiter's aurora observed by Hisaki/EXCEED: 3. Volcanic control of Jupiter's aurora. *Geophysical Research Letters*, *45*, 71–79. https//doi.org/10.1002/2017GL075814

Tao, C., Miyoshi, Y., Achilleos, N., & Kita, H. (2014). Response of the Jovian thermosphere to variations in solar EUV flux. *Journal of Geophysical Research: Space Physics*, *119*, 3664–3682. https//doi.org/10.1002/2013JA019411

Waite, J. H., Cravens, T. E., Kozyra, J., Nagy, A. F., Atreya, S. K., & Chen, R. H. (1983). Electron precipitation and related aeronomy of the Jovian thermosphere and ionosphere. *Journal of Geophysical Research*, *88*, 6143–6163. https//doi.org/10.1029/JA088iA08p06143

Yates, J. N., Achilleos, N., & Guio, P. (2012). Influence of upstream solar wind on thermospheric flows at Jupiter. *Planetary and Space Science*, *61*, 15–31. https//doi.org/10.1016/j.pss.2011.08.007

Yates, J. N., Achilleos, N., & Guio, P. (2014). Response of the Jovian thermosphere to a transient "pulse" in solar wind pressure. *Planetary and Space Science*, *91*, 27–44. https//doi.org/10.1016/j.pss.2013.11.009

Yates, J. N., Ray, L. C., & Achilleos, N. (2018). An initial study into the long-term influence of solar wind dynamic pressure on Jupiter's thermosphere. *Journal of Geophysical Research: Space Physics*, *123*, 9357–9369. https//doi.org/10.1029/2018JA025828

Yelle, R. V., & Miller, S. (2004). *Jupiter's thermosphere and ionosphere* (pp. 185–218). Cambridge, UK: Cambridge University Press.

Yelle, R. V., Young, L. A., Vervack, R. J., Young, R., Pfister, L., & Sandel, B. R. (1996). Structure of Jupiter's upper atmosphere: Predictions for Galileo. *Journal of Geophysical Research*, *101*, 2149–2162. https//doi.org/10.1029/95JE03384

Young, L. A., Yelle, R. V., Young, R., Seiff, A., & Kirk, D. B. (1997). Gravity waves in Jupiter's thermosphere. *Science*, *276*, 108–111. https//doi.org/10.1126/science.276.5309.108